

A Model for AR Scorpii: Emission from relativistic electrons trapped by closed magnetic field lines of magnetic white dwarfs

Takata, J.¹, Yang, H.¹

and

Cheng, K.S.²

takata@hust.edu.cn

hrspksc@hku.hk

ABSTRACT

AR Scorpii is an intermediate polar system composed of a magnetic white dwarf (WD) and an M-type star, and shows non-thermal, pulsed, and highly linearly polarized emission. The radio/optical emission modulates with the WD's spin and show the double peak structure in the light curves. In this paper, we discuss a possible scenario for the radiation mechanism of AR Scorpii. The magnetic interaction on the surface of the companion star produces an outflow from the companion star, the heating of the companion star surface, and the acceleration of electrons to a relativistic energy. The accelerated electrons, whose typical Lorentz factor is $\sim 50 - 100$, from the companion star move along the magnetic field lines toward the WD surface. The electrons injected with the pitch angle of $\sin \theta_{p,0} > 0.05$ are subject to the magnetic mirror effect and are trapped in the closed magnetic field line region. We find that the emission from the first magnetic mirror points mainly contributes to the observed pulsed emission and the formation of the double-peak structure in the light curve. For the inclined rotator, the pulse peak in the calculated light curve shifts the position in the spin phase, and a Fourier analysis exhibits a beat frequency feature, which are consistent with the optical/UV observations. The pulse profile also evolves with the orbital phase owing to the effect of the viewing geometry. The model also interprets the global features of the observed spectral energy distribution in radio to X-ray energy bands. We also discuss the curvature radiation and the inverse-Compton scattering process in the outer gap accelerator of the WD in AR Scorpii and discuss the possibility of the detection by future high-energy missions.

¹School of Physics, Huazhong University of Science and Technology, Wuhan 430074, China

²Department of Physics, The University of Hong Kong, Pokfulam Road, Hong Kong

1. Introduction

White dwarf (hereafter WD) is the end point of the stellar evolution of a progenitor with a mass of $M \leq 8M_{\odot}$, and for over 97% of all stars. There are WDs with a strong magnetic field in the range of $B_s \sim 10^3 - 10^9$ G, which has been determined by the polarization and/or Zeeman splitting, and the WD belonging to this class is called a *magnetic WD* (Ferrario et al. 2015). The first magnetic WD, Grw+70°8247 with $B_s = 100 - 300$ MG, was reported in the 1970s (Kemp et al. 1970; Angel et al. 1985), and it is located about 13 pc (43 lt-yr) away. The number of the magnetic WDs is rapidly increased by the Sloan Digital Sky Survey (SDSS; York et al. 2000; Kepler et al. 2013). The WD catalog based on the SDSS DR7 (c.f. Kleinman et al. 2013) includes 19713 WDs, in which ~ 12831 is the hydrogen atmosphere WD (called DAs). Among the DAs listed in SDSS-DR7, Kepler et al. (2013) measured the Zeeman splitting from $\sim 4\%$ (521) of all DAs observed and estimated the surface magnetic field at $B_s = 1 \sim 700$ MG. In the SDSS DR10, Kepler et al. (2015) discovered 9089 new WDs, including 206 magnetic WDs. Although the volume density of magnetic WDs is still unknown, these observations would suggest that 5–10% of the WDs are magnetic WDs (Sion et al. 2014; Kepler et al. 2015). The space density of the WDs estimated as $5 \times 10^{-3} \text{pc}^{-3}$ by the direct measurement of local WDs (Holberg 2002 and references therein) suggests that a large number of the magnetic WDs are existing in the galaxy.

A magnetic WD is observed as an isolated system or a binary system, and the highly magnetic WD is found in the binary system, which is known as cataclysmic variable (hereafter CV). The CVs usually accrete matter on the WDs from the late-type main-sequence companion through Roche lobe overflow, and the magnetic CVs compose $\sim 20\%$ of all CVs (~ 1100 CVs; Ritter & Kolb 2010). The magnetic CV is mainly divided into two groups, that is, polar and intermediate polar system (IP). The WD of the polar has a surface magnetic field of $B_s > 10$ MG, which is sufficiently large to lock the two stars into synchronous rotation with the orbital period ($P_{obs} \sim 100 - 500$ minutes, Ferrario et al. 2015). The WD in the IP has a smaller surface magnetic field $B_s \sim 0.1 - 10$ MG than that in the polar. The magnetic field of WDs is not sufficient to lock the companion into the synchronous rotation, and the spin of the WD is observed with a shorter period than the orbital period. Both polars and IPs emit X-rays owing to accretion of the matter from the companion on the WD’s surface.

Since the synchronous rotation of two stars in polar, there is no angular momentum of the accreting matter relative to the WD, and the formation of the accretion disk is prevented. For the IPs, the accretion disk can present, and the angular momentum transfer by the disk matter will spin up the magnetic WD. The accretion process on the compact object is discussed with the so-called co-rotation radius, $r_{co} = (GM_{WD}P_{WD}^2/4\pi^2)^{1/3}$, where the WD’s spin frequency is equal to the disk rotation frequency (Keplerian frequency), and the Alfvén

radius, $r_M = 3 \times 10^{10} \dot{M}_{16}^{-2/7} M_{WD,1}^{-1/4} \mu_{WD,33}^{4/7} \text{cm}$ (Frank et al. 2002), where the magnetic pressure of the WD is equal to the dynamic pressure of the accretion disk. Here M_{WD} is the mass of the WD, $M_{WD,1} = M_{WD}/M_\odot$, \dot{M}_{16} is the accretion rate in units of 10^{16}g s^{-1} and $\mu_{WD,33}$ is the dipole moment of the WD in units of 10^{33}G cm^3 . When $r_M < r_{co}$, the inner edge of the accretion disk can enter inside the co-rotation radius and the disk matter can accrete onto the compact object. Then, the condition of the accretion through the disk may be written down as $\dot{M}_{16} \geq P_{WD,h}^{-7/3} \mu_{WD,33}^2 M_{WD,1}^{-49/24}$, where $P_{WD,h} = P_{WD}/1\text{hour}$.

Some WDs in the IPs are rapidly rotating with a period $P_{WD} < 100\text{s}$ (Ferrario et al. 2015, and reference therein): $P_{WD} = 33.1\text{s}$ for AE Aquarii (AE Aqr), 70.8s for DQ Her, and 67.6s for V455 And. For those magnetic WDs, an accretion rate close to the Eddington rate $\dot{M}_E \sim 10^{20} \text{g/s}$ is necessary to satisfy the condition ($r_M < r_c$) for the formation of the accretion disk. However, the time-averaged rate of the mass transfer from the companion is observed with $\dot{M}_{16} = 1 - 100$ (Patterson 1994) for those systems, suggesting that these systems will not contain the disk, and probably the matter from Roche lobe directly streams toward the WD surface, or most of the matter from the companion is centrifugally ejected (propeller phase). In fact, the Doppler tomography profile of the AE Aqr (e.g. Wynn et al. 1997) indicates that the AE Aqr is in the propeller phase (Ikhsanov et al. 2004). Moreover, the pulse timing study of the AE Aqr revealed that the WD is spinning down at a rate of $\dot{P}_{WD} \sim 5.64 \times 10^{-14}$ (de Jager et al. 1994), corresponding to a spin-down luminosity of $L_{sd} = I(2\pi)^2 \dot{P}_{WD}/P_{WD}^3 \sim 6 \times 10^{33} I_{50} \text{erg/s}$, where I_{50} is the WD's moment of inertia in units of 10^{50}g cm^2 . Because of the low mass accretion rate with the high spin-down rate, the AE Aqr has been considered as the first WD pulsar candidate that operates the mechanisms of the neutron star (NS) pulsar-like particle acceleration and the non-thermal radiation process in the magnetosphere.

The mechanism of the NS pulsar-like particle acceleration in the magnetosphere of the magnetic WD has been discussed by several authors (Usov 1988; Ikhsanov 1998; Kashiyama et al. 2011). In the model, an electron (or a positron) that emerged from the polar cap region is accelerated by an electric field parallel to the open magnetic field lines. The electric potential difference across the open field lines is estimated by

$$V_a = (2\pi)^2 \frac{\mu_{WD}}{2c^2 P_{WD}^2} \sim 6 \times 10^{13} \left(\frac{\mu_{WD}}{10^{34} \text{G cm}^3} \right) \left(\frac{P_{WD}}{33\text{s}} \right)^{-2} \text{ static Volt}, \quad (1)$$

which can accelerate the electron up to $\gamma_{max} \sim eV_a/m_e c^2 \sim 10^8 \mu_{WD,34} (P_{WD}/33\text{s})^{-2}$. This relativistic electron emits the nonthermal photon via the curvature radiation process with a characteristic energy of

$$E_\gamma = \frac{3}{4\pi} \frac{hc\gamma^3}{R_c} \sim 200 \text{MeV} \left(\frac{\gamma}{10^8} \right)^3 \left(\frac{P}{33\text{s}} \right)^{-1} \left(\frac{R_c}{\varpi_{lc}} \right)^{-1}, \quad (2)$$

where R_c is the curvature radius of the magnetic field line and $\varpi_{lc} = cP_{WD}/2\pi$ is the light-cylinder radius. Kashiyama et al. (2010) discussed the mechanism of the NS pulsar-like pair-creation process in the magnetic WD magnetosphere as the possible source of the cosmic-ray electrons and positrons. Although very high energy emission (de Jager 1994) and nonthermal X-ray emission (Terada et al. 2008) from AE Aqr were reported, the observational view on the WD pulsar has not been firmly established. In section 4, we will discuss the NS pulsar-like high-energy emission process of the magnetic WD.

New discovery of the pulsed radio/optical/UV emission from AR Scorpii (hereafter AR Sco) sheds light on the nonthermal nature of the magnetic WD (Marsh et al. 2016). AR Sco is the IP with an orbital period of $P_o \sim 3.56\text{hr}$, and it is composed of an M star ($M_2 \sim 0.3M_\odot$ and $R_2 \sim 0.3R_\odot$) and a magnetic WD. The interesting properties of the emission from AR Sco are the nonthermal, pulsed, and highly linearly polarized emission. The radio/optical/UV emission modulates periodically on a period of $P \sim 1.97\text{minutes}$, which is thought to be the spin period of the magnetic WD. The double-peak structure of the pulse profile and the morphology of the linear polarization (Buckely et al. 2017) in the optical bands are resemble to those of the Crab pulsar, which is the isolated young NS pulsar and emits the electromagnetic waves in radio to high-energy TeV bands (Kuiper et al. 2001; Kanbach et al. 2005; Takata et al. 2007). Moreover, the optical emission also modulates on the orbital period (3.56hr), which will reflect the heating of the dayside of the companion star by the interaction of the magnetic field/radiation by the WD. The modulation of the optical emission from the companion star with the orbital motion is also similar to that of the millisecond NS pulsar/low-mass star binary system (Fruchter et al. 1988; Kong et al. 2012).

AR Sco’s broadband electromagnetic spectrum in radio to X-ray bands is characterized by the synchrotron radiation from the relativistic electrons, indicating the acceleration process in the magnetosphere of the WD. As pointed out by Geng et al. (2016), on the other hand, the number of the particles that emit the observed nonthermal optical emission of AR Sco is significantly larger than the number that can be supplied by the WD itself. This suggests that the synchrotron-emitting electrons are supplied from the companion star’s surface, and the acceleration process is different from that of the NS pulsar. Geng et al. (2016) suggested an electron/position beam from the WD’s polar cap sweeping the stellar wind from the companion star, and a bow shock propagating into stellar wind accelerates the electrons in the wind.

Geng et al. (2016) discussed the emission due to the interaction between the companion star and the WD’s open magnetic field lines that extend beyond the light cylinder ($\varpi_{lc} = 5.6 \times 10^{11}\text{cm}$), and hence assumed that the WD is a nearly perpendicular rotator. In this

paper, we investigate another possibility that the electrons accelerated around the companion stellar surface are trapped by the close magnetic field lines of the WD. The injected electrons from the stellar surface are accelerated at the vicinity of the companion star and initially travel toward the WD’s surface along the magnetic field line. We will solve the evolution of the pitch angle of such electrons under the effects of the synchrotron radiation energy-loss and the first adiabatic invariance. In section 2, we will describe our model and the basic equation for the motion of the trapped electrons. We also discuss the direction of the emission by the relativistic electrons to calculate the light curve. In section 3, we will show our results and discuss the mirror effect of the electron’s motion. We also show the model pulse profile in optical and X-ray bands. In section 4, we discuss the particle acceleration and the high-energy emission from the outer gap accelerator of the WD in AR Sco and will calculate the expected fluxes of the curvature radiation process and the inverse-Compton scattering (hereafter IC) process.

2. Theoretical Model

2.1. Energy injection

In this section, we will discuss the emission model for the observed radio/optical/X-ray emission from AR Sco. The WD’s magnetic field lines sweep periodically across the surface of the companion star. The strength of the magnetic field of the WD at the surface of the companion star will be of the order of

$$B_{WD} \sim 195 \left(\frac{\mu_{WD}}{10^{35} \text{Gcm}^3} \right) \left(\frac{a}{8 \cdot 10^{10} \text{cm}} \right)^{-3} \text{G}. \quad (3)$$

The modulation of the optical emission with the orbital period ($\sim 3.56\text{hr}$) indicates that the spinning of the secondary star is synchronized with the orbital motion. With such a rapidly spinning M star, the stellar dynamo process can generate a polar magnetic field of several kG (Reiners et al. 2009). A magnetic interaction between the WD and M star will cause the magnetic reconnection or ohmic dissipation, and the dissipated magnetic energy will be used for (1) the heating of the M star surface, (2) acceleration of the electrons, and (3) outflow from the M star.

The magnetic interaction will produce an azimuthal component (δB_ϕ) of the magnetic field of the WD, and its pitch $\eta = \delta B_\phi / B$ may increase at $\eta \rightarrow 1$ before the magnetic field becomes unstable against the magnetic dissipation process. In this model, we estimate the

power of the magnetic dissipation as (Lai 2012; Buckley et al. 2017 and references therein)

$$L_B = \frac{\eta B^2}{8\pi} (4\pi R_2^3 \delta) \Omega_{WD} \sim 2.8 \times 10^{32} \text{erg/s} \\ \times \left(\frac{\mu_{WD}}{10^{35} \text{G cm}^3} \right)^2 \eta \left(\frac{\delta}{0.01} \right) \left(\frac{R_2}{3 \cdot 10^{10} \text{cm}} \right)^3 \left(\frac{a}{8 \cdot 10^{18} \text{cm}} \right)^{-6} \left(\frac{P_{WD}}{117 \text{s}} \right), \quad (4)$$

where $\Omega_{WD} = 2\pi/P_{WD}$, R_2 is the radius of the M star, and $\delta \sim 0.01$ is the skin depth (see Buckley et al. 2017).

The magnetic interaction on the companion surface may eventually cause an ablation of the matter from the M star surface and an acceleration of the electrons to the relativistic energy. The ablation of the companion star by the WD magnetic field could occur if the binary is close enough so that an energy deposition on the envelope of the stellar surface is high. The ablation of the companion star by the deposition of the electromagnetic energy is a common process for the millisecond NS pulsar and low-mass companion star binary, which is called as black widow/redback pulsars (Roberts 2013). In the black widow/redback systems, it has been observed that most of the deposited energy on the stellar surface is converted into the heating of the companion star surface and/or the nonthermal radiation process, and a tiny fraction (0.1-1%) of it is used for the ablation of the matter from the companion star (van den Heuvel & Paradijs 1988; Cheng 1989). Since the mass loss driven by the irradiation from the compact star has not been well understood, we introduce the efficiency factor χ for converting the dissipated energy into the kinetic energy of the wind,

$$\chi = \frac{\dot{M} v_{esc}^2 / 2}{L_B}. \quad (5)$$

For the black widow/redback system, the efficiency factor has been estimated as $\chi \sim 0.01 - 0.001$.

In terms of the efficiency factor, we estimate the rate of the particles leaving from the companion star surface as

$$\dot{N}_p \sim \frac{\dot{M}}{m_p} = \frac{\chi L_B}{\frac{1}{2} m_p v_{esc}^2} \\ \sim 5 \times 10^{40} \chi \left(\frac{L_B}{10^{32} \text{erg/s}} \right) \left(\frac{v_{esc}}{5 \cdot 10^7 \text{cm/s}} \right)^{-2} / \text{s}, \quad (6)$$

where $v_{esc} = \sqrt{2GM_2/R_2}$ is the escape velocity, with $M_2 (\sim 0.3M_\odot)$ being the mass of the companion star. Because of the charge conservation, we assume that the number of the electrons that leave from the stellar surface and that are accelerated by the magnetic dissipation process is of the order of $\dot{N}_e = \dot{N}_p$.

In this model, we assume that most of the dissipated magnetic energy is used for the acceleration of the electrons and/or the heating of the companion surface. Hence, the typical Lorentz factor of the accelerated electrons may be estimated to be

$$\begin{aligned}\gamma_0 &\sim \frac{L_B}{\dot{N}_e m_e c^2} = \frac{m_p v_{esc}^2}{2\chi m_e c^2} \\ &\sim 50 \left(\frac{\chi}{5 \cdot 10^{-5}} \right)^{-1} \left(\frac{v_{esc}}{5 \cdot 10^7 \text{cm/s}} \right),\end{aligned}\tag{7}$$

where $\chi \sim 10^{-5}$ will be chosen to fit the observed luminosity and SED of AR Sco.

2.2. Motion of trapped electron

In AR Sco, the light cylinder of the WD is $\varpi_{lc} \sim 5.6 \times 10^{11} \text{cm}$, which is larger than the separation ($a \sim 8 \times 10^{10} \text{cm}$) between two stars. Hence, the companion star will interact with the close magnetic field lines of the WD, unless the WD is a nearly perpendicular rotator. As we discuss above, the magnetic interaction between the closed magnetic field of the WD and the companion star will produce the pitch $\delta B_\phi/B \sim 1$ for the WD and will cause the magnetic reconnection/dissipation, which accelerates the electrons. After sweeping across the companion star surface, the magnetic field line of the WD will remain to be closed, and the injected electrons may be trapped at the closed magnetic field lines by the magnetic mirror effect. Since the radius of the gyration motion of an electron is much smaller than the size of the magnetosphere, $r_{gy} \sim 440 \text{cm} (\mu_{WD}/10^{35} \text{G cm}^3)^{-1} (\gamma_0/50)$, we ignore any drift motion crossing the magnetic field lines in the *co-rotating frame* of the WD, that is, in the laboratory frame, the trapped electron is co-rotating with the WD by the $\vec{E} \times \vec{B}$ drift, and it moves only along the magnetic field line.

We expect that the observed optical emission from AR Sco is produced by the electron with the typical Lorentz factor $\gamma_0 \sim 50$ of equation (7). With the typical Lorentz factor $\gamma_0 \sim 50$, on the other hand, the time scale of the synchrotron loss around the companion star is estimated as

$$\tau_{syn} \sim 400 \text{s} \left(\frac{\mu_{WD}}{10^{35} \text{G cm}^3} \right)^{-2} \left(\frac{a}{8 \cdot 10^{10} \text{cm}} \right)^6 \left(\frac{\gamma_0}{50} \right)^{-1},$$

which is longer than the crossing time scale of $a/c \sim 2.5 \text{s}$. This indicates that the injected electrons do not lose their energy around the companion star, and they migrate into the inner magnetosphere before the synchrotron energy-loss. For the electrons moving toward the WD surface, the increase in the perpendicular momentum due to the first adiabatic invariance competes with the decrease in it due to the synchrotron loss.

The evolution of the Lorentz factor and the pitch angle along the magnetic field line under the synchrotron energy-loss and the first adiabatic invariance may be described by (Harding et al. 2005)

$$\frac{d\gamma}{dt} = -\frac{P_{\perp}^2}{t_s}, \quad (8)$$

and

$$\frac{d}{dt} \left(\frac{P_{\perp}^2}{B} \right) = -2 \frac{B}{t_s \gamma} \left(\frac{P_{\perp}^2}{B} \right)^2, \quad (9)$$

where B is the local magnetic field strength, $t_s = 3m_e^3 c^5 / (2e^4 B^2)$, and $P_{\perp} = \gamma \beta \sin \theta_p$ with $\beta = v/c$ and θ_p the pitch angle. To solve above equations, we apply the pure dipole magnetic field of

$$\vec{B} = \frac{3\vec{n}_p(\vec{n}_p \cdot \vec{\mu}_{WD}) - \vec{\mu}_{WD}}{r^3}, \quad (10)$$

where \vec{n}_p is the unit vector of the position. In this paper, α denotes the angle between the spin axis and the magnetic axis of the WD.

When the synchrotron loss time scale is much longer than the crossing time scale, the perpendicular momentum of the electrons moving toward the WD surface from the companion star increases as

$$P_{\perp}(r) = \left(\frac{a}{r} \right)^{3/2} P_{\perp,0}, \quad (11)$$

where $P_{\perp,0}$ is the initial perpendicular momentum. The magnetic mirror could occur at the point

$$r_m \sim a \sin^{2/3} \theta_{p,0} \quad (12)$$

where $\theta_{p,0}$ is the initial pitch angle, provided that the crossing time scale $\tau_{m,c} = r_m/c$ is shorter than the synchrotron loss time scale at r_m , $\tau_{m,syn} = 3m_e^3 c^5 a^6 \sin^2 \theta_{p,0} / (2e^4 \mu_{WD}^2 \gamma_0)$. From the inequality $\tau_{m,syn} > \tau_{m,c}$, the critical initial pitch angle, above which the electron is subject to the magnetic mirroring, may be written as

$$\begin{aligned} \sin \theta_{p,0} &> \left(\frac{2e^4 \mu_{WD}^2 \gamma}{3m_e^3 c^6 a^5} \right)^{3/4} \\ &\sim 0.03 \left(\frac{\mu_{WD}}{10^{35} \text{Gcm}^3} \right)^{3/2} \left(\frac{\gamma_0}{50} \right)^{3/4} \left(\frac{a}{8 \cdot 10^{10} \text{cm}} \right)^{-15/4}. \end{aligned} \quad (13)$$

2.3. Radiation Process

Besides the IR/optical/UV emission, the AR Sco is also observed in the X-ray bands, and this will indicate that the electrons with a Lorentz factor larger than $\gamma_0 \sim 50$ exist in the magnetosphere of the WD. To explain the X-ray emission, we assume that a process related

to the magnetic dissipation on the companion star surface accelerates the electrons to the relativistic speed and forms a power-law distribution of the electrons over several decays in energy:

$$f(\gamma) = K_0 \gamma^{-p}, \quad \gamma_{min} \leq \gamma \leq \gamma_{max}, \quad (14)$$

where we use $\gamma_{min} = \gamma_0$ of equation (7). For the maximum Lorentz factor of the accelerated particle is determined as the Lorentz factor at which the synchrotron cooling timescale $\tau_s \sim 9m_e^3 c^5 / (4e^4 B^2 \gamma)$ is equal to the acceleration timescale $t_a \sim \gamma m_e c / (\xi e B)$, yielding $\gamma_{max} \sim 8 \times 10^6 \xi^{1/2} (\mu_{WD} / 10^{35} \text{Gcm}^3)^{-1/2} (a / 8 \cdot 10^{10} \text{cm})^{1/2}$, where $\xi < 1$ represents the efficiency of the acceleration. By assuming the power-law index of $p \sim 2.5$, which is a fitting parameter, we calculate the normalization (K_0) and the minimum Lorentz factor by solving the conditions that $\int f(\gamma) d\gamma = \dot{N}_e$ and $\int \gamma m_e c^2 f(\gamma) d\gamma = L_B$. The spectrum of the synchrotron radiation at the photon energy E_s is calculated from

$$P_{syn}(E_s) = \frac{\sqrt{3} e^2 B \sin \theta_p}{h m_e c^2} F_{sy} \left(\frac{E_s}{E_{syn}} \right), \quad (15)$$

where h is the Plank constant, $E_{syn} = 3 h e \gamma^2 B \sin \theta_p / (4 \pi m_e c)$ is the typical photon energy, and $F_{sy}(x) = x \int_0^\infty K_{5/3}(y) dy$ with $K_{5/3}$ being the modified Bessel function of the order 5/3.

2.4. Radiation direction

To investigate the expected modulation of the observed emission with the WD's spin, we calculate the propagation direction and the time of arrival (TOA) of each emitted photon. For the coordinate system, we introduce the z -axis at the spin axis of the WD and also assume that the spin axis of the WD and orbital axis are aligned for simplicity. The x -axis is chosen so that the observer is located at the first quadrant in the (x, z) coordinate (Figure 1). The direction of the magnetic momentum $\vec{\mu}_{WD}$ (the magnetic axis) is inclined by α from the z -axis, and it is rotating around the z -axis.

For a high Lorentz factor, we can anticipate that the emission direction of the particles coincides with the direction of the particle's velocity. In the laboratory frame, the unit vector of the electron motion that is co-rotating with the WD may be described by (Takata et al. 2007)

$$\vec{n}_e = \beta_0 \cos \theta_p \vec{b} + \beta_0 \sin \theta_p \vec{b}_\perp + \beta_{co} \vec{e}_\phi, \quad (16)$$

where the first, second, and third terms on the right-hand side represent the motion along the magnetic field line, the gyration motion, and the co-rotation motion, respectively. The value of the parallel speed β_0 in equation (16) at each point is calculated from the conditions that $|\vec{n}_e| = 1$ and $\beta_{co} = \varpi / \varpi_{lc}$, where ϖ is the axial distance from the spin axis of the WD.

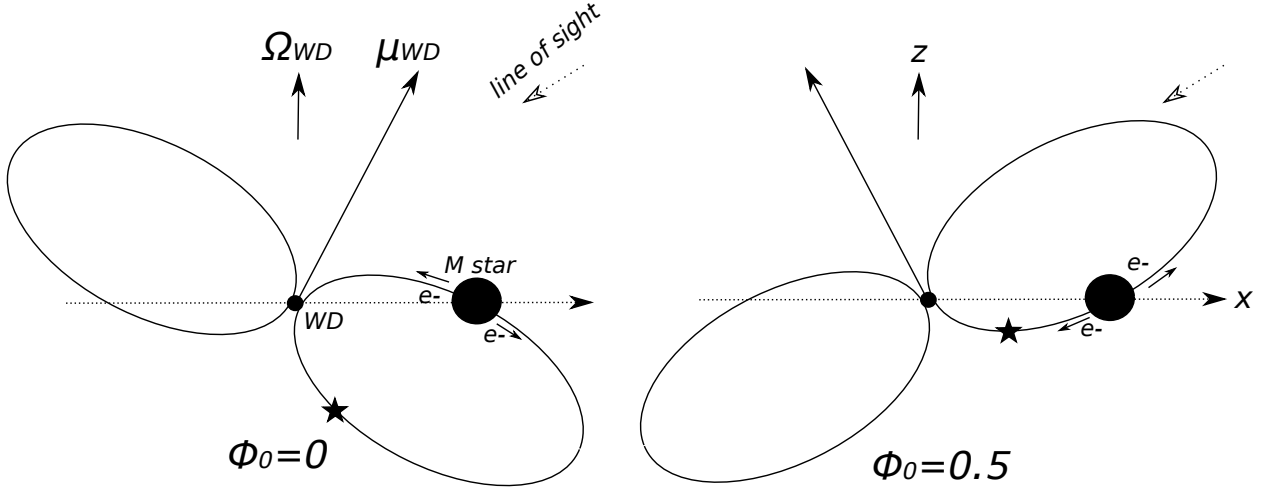


Fig. 1.— Schematic view of the AR Sco system and the coordinate in the study. The observer is located within the plane made by the spin-axis (z-axis) and x-axis. The spin phase zero Φ_0 is defined as when the magnetic axis points toward the observer. In the figure, the M star is assumed to be located at the plan by the spin axis and x-axis. The electrons are injected from the companion star by the magnetic field interaction. The star symbols represent position of the first magnetic mirror point of the electrons injected into the southern hemisphere. The travel time to the first magnetic mirror point is shorter for the electron injected at $\Phi_0 = 0.5$ than those injected at $\Phi_0 = 0$ (see section 3.2).

In addition, the vectors $\vec{b} = \vec{B}/B$, \vec{b}_\perp , and \vec{e}_ϕ are the unit vectors along the magnetic field line, perpendicular to the magnetic field line, and in the azimuthal direction, respectively. The unit vector b_\perp is defined by

$$\vec{b}_\perp = \cos \delta\phi_g \vec{k} + \sin \delta\phi_g \vec{b} \times \vec{k}, \quad (17)$$

where \vec{k} is any unit vector perpendicular to the magnetic field line and $\delta\phi_g$ refers to the phase of the gyration motion.

The emission direction of equation (16) is interpreted as the angle measured from the rotation axis, $\zeta = \cos^{-1} n_{e,z}$, where $n_{e,z}$ is the component of the emission direction along the rotation axis and the azimuthal angle ϕ measured from the x -axis. Since the observer is laid on the first quadrant of the plane made by the x -axis and z -axis (Figure 1), we pick up the photon traveling in the direction $\phi = 0$ to calculate the pulse profile.

The TOA of the emitted photon measured on the Earth may be expressed by

$$\text{TOA} = t_{\Phi_0} + \delta t_{emi} + \frac{D - \vec{r} \cdot \vec{n}_e}{c},$$

where D is the distance to the source. The first, second, and third terms on the right-hand side represent the time of the injection of the relativistic electron into the WD magnetosphere, the travel time of the electron to the emission point after the injection, and the flight time of the emitted photon from the emission point (\vec{r}) to the Earth, respectively. We can safely ignore the effect of the flight time due to the orbital motion of the WD, since it will be $\delta t \ll a/c \sim 2\text{s}$, which is much smaller than the spin period. The TOA can be translated into the spin phase of WD as

$$\Phi = \Phi_0 + 2\pi \frac{\delta t_{emi}}{P_{WD}} - \frac{\vec{r} \cdot \vec{n}_e}{\varpi_{lc}}, \quad (18)$$

where Φ is the spin phase at the detection of photon and Φ_0 is the spin phase at the injection of electrons. In this paper, we define $\Phi_0 = 0$ as the time when the WD's magnetic axis is oriented in the plane made by WD's rotation axis and the observer (Figure 1). We note that the second term on the right-hand side does not appear if the high-energy electrons are continuously injected on the same magnetic field line with time, such as the high-energy emission from the NS pulsar (Takata et al 2007). Moreover, since the main emission region is located at the position $r \ll a = 8 \times 10^{10}\text{cm}$, the third term on the right-hand side, $\sim r/\varpi_{lc} \ll a/\varpi_{lc} \sim 0.14$, is negligible, while it is important to produce the sharp pulse in the light curve of the high-energy emission from the NS pulsar.

3. Results

We treat the companion star as the point object located at $r = a = 8 \times 10^{10}\text{cm}$ and on the equator of the WD, for simplicity. This may be a rough treatment for this system, since the size of the companion star is not negligible compared to the size of the orbital separation. However, we expect that the main results discussed in this paper will not be modified even if we take into account the size of the companion star. Under this assumption, we evaluate the magnetic energy dissipation and the injection of the electrons at the companion star.

3.1. Magnetic mirror effect

Figures 2 and 3 represent the evolution of the Lorentz factor and the perpendicular momentum (P_{\perp}) calculated from equations (8) and (9). In the calculations, the electron with the initial Lorentz factor $\gamma_0 = 50$ and the sine of the pitch angle $\sin \theta_0 = 0.1$ for Figure 2 or $\sin \theta_0 = 0.05$ for Figure 3 is injected toward the WD surface from $r = a = 8 \times 10^{10}\text{cm}$. We assume the magnetic dipole field with $\mu_{WD} = 6.5 \times 10^{34}\text{G cm}^3$ and the inclination angle of $\alpha = 0^\circ$.

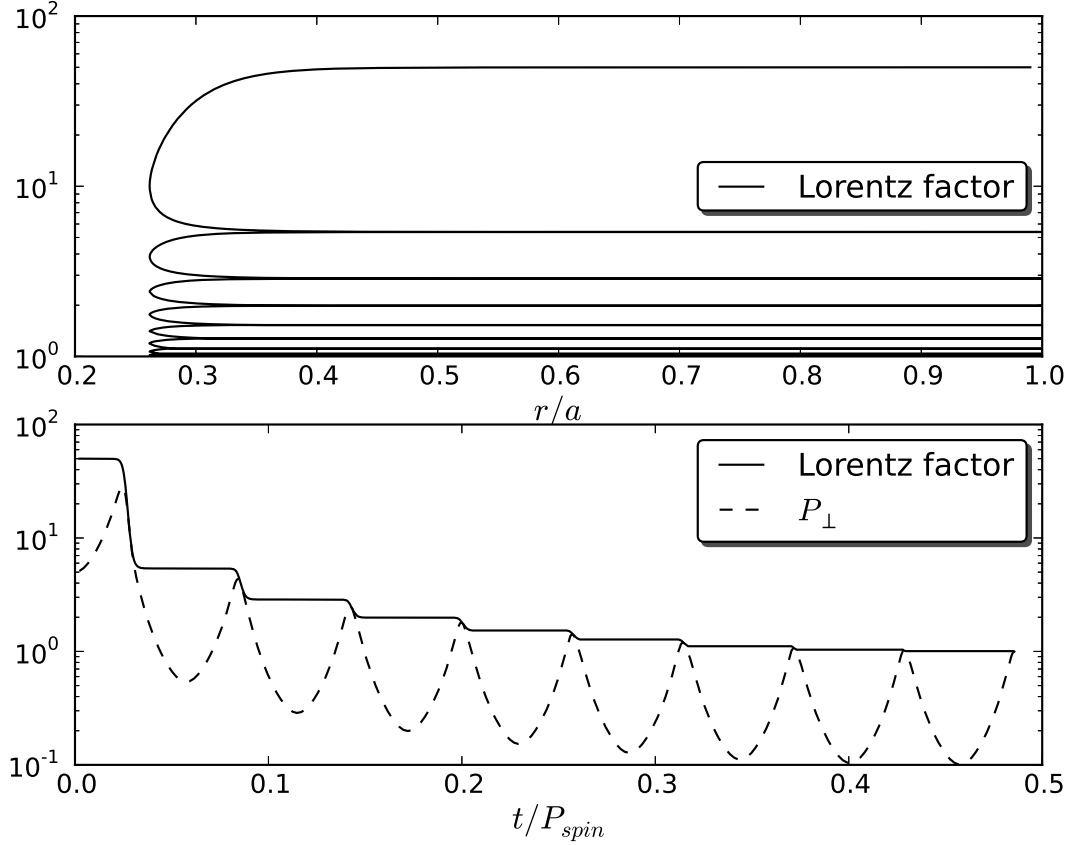


Fig. 2.— Trajectory of the electron calculated from equations (8) and (9). Top panel: evolution of Lorentz factor along the radial distance. Bottom panel: evolution of Lorentz factor and perpendicular momentum (P_{\perp}) as a function of time. The magnetic field of the WD is assumed to be the pure dipole field with $\mu_{WD} = 6.5 \times 10^{34} \text{G cm}^3$, and the magnetic axis is aligned with the spinning axis ($\alpha = 0^\circ$). The electron with the pitch angle $\sin \theta_{p,0} = 0.1$ and the Lorentz factor $\gamma_0 = 50$ is injected from $r/a = 1$ ($t/P_{WD} = 0$) and the equator. The electron is trapped at the close magnetic field line by the magnetic mirror.

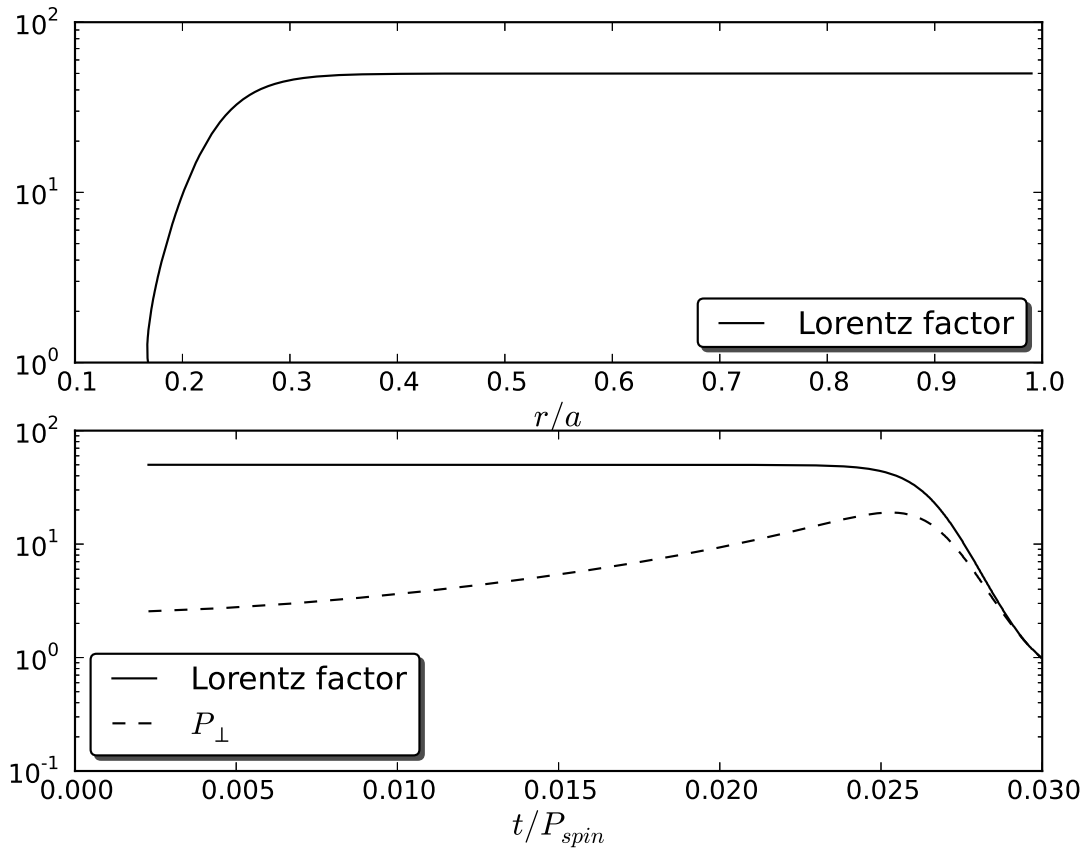


Fig. 3.— Same as Figure 2, but $\sin \theta_{p,0} = 0.05$. The electron is not trapped by the magnetic mirror.

The top panel of Figure 2 shows the evolution of the Lorentz factor as a function of the radial distance and indicates that the injected electron is trapped at $\sim 0.25 < r/a < 1$ by the magnetic mirror effect. At around $r \sim a$, the synchrotron cooling time scale is longer than the dynamical time scale $\sim a/c$, and the electron migrates toward the WD with an almost constant Lorentz factor. As the dotted line in the bottom panel of Figure 2 shows, the perpendicular momentum P_{\perp} increases with a time owing to the first adiabatic invariance. Around the magnetic mirror point, where the pitch angle becomes $\sin \theta_p \sim 1$, the synchrotron energy-loss increases, and it rapidly decreases the Lorentz factor. After the magnetic mirror, the electron moves toward the outer magnetosphere with the synchrotron loss time scale longer than the dynamical time scale, and hence the Lorentz factor is almost constant. Since the electron travels on the closed magnetic field lines, it eventually moves toward WD’s surface in another hemisphere and is reflected back again by the magnetic mirror. As Figure 2 indicates, most of the initial energy of the electron injected with $\sin \theta_{p,0} = 0.1$ is lost by the synchrotron radiation at the first magnetic mirror point.

For the smaller initial pitch angle of $\sin \theta_{p,0} = 0.05$ in Figure 3, the electrons can enter the inner magnetosphere, and the stronger synchrotron energy-loss prevents the magnetic mirror. The top left panel of Figure 4 represents the evolution of the Lorentz factor as a function of the time from the injection. The figure indicates that the electron injected with the small pitch angle of $\sin \theta_{p,0} = 0.1$ (solid line) radiates away all the initial energy within a timescale less than the spin period, while for the electron with a larger pitch angle $\sin \theta_{p,0} = 0.2$ (dashed line) and 0.5 (dotted line), the energy-loss time scale is longer than the spin period of the WD.

3.2. Formation of the pulse

Figure 4 shows the sky map of the angle (ζ) and the spin phase (Φ) for the emission from the electron injected at $\Phi_0 = 0$ with the Lorentz factor $\gamma_0 = 50$ and the pitch angle $\sin \theta_{p,0} = 0.1$ (top right), 0.2 (bottom left), and 0.5 (bottom right); the brightness of the color in the figure refers the observed intensity. With $\gamma_0 = 50$, the electrons injected with $\sin \theta_{p,0} \geq 0.1$ are subjected to the magnetic mirror, as the top left panel of Figure 4 indicates, and the synchrotron energy-loss mainly occurs at the magnetic mirror point. Around the magnetic mirror point, the pitch angle of the electron is increased to 90 degree, and the gyration motion produces the synchrotron beam that covers the large region in the angle ζ , as we can see in Figure 4.

As we can also see in Figure 4, the sky map of the observed emission from one electron depends on the initial pitch angle. For the injected electron with $\sin \theta_{p,0} = 0.1$ (see top right

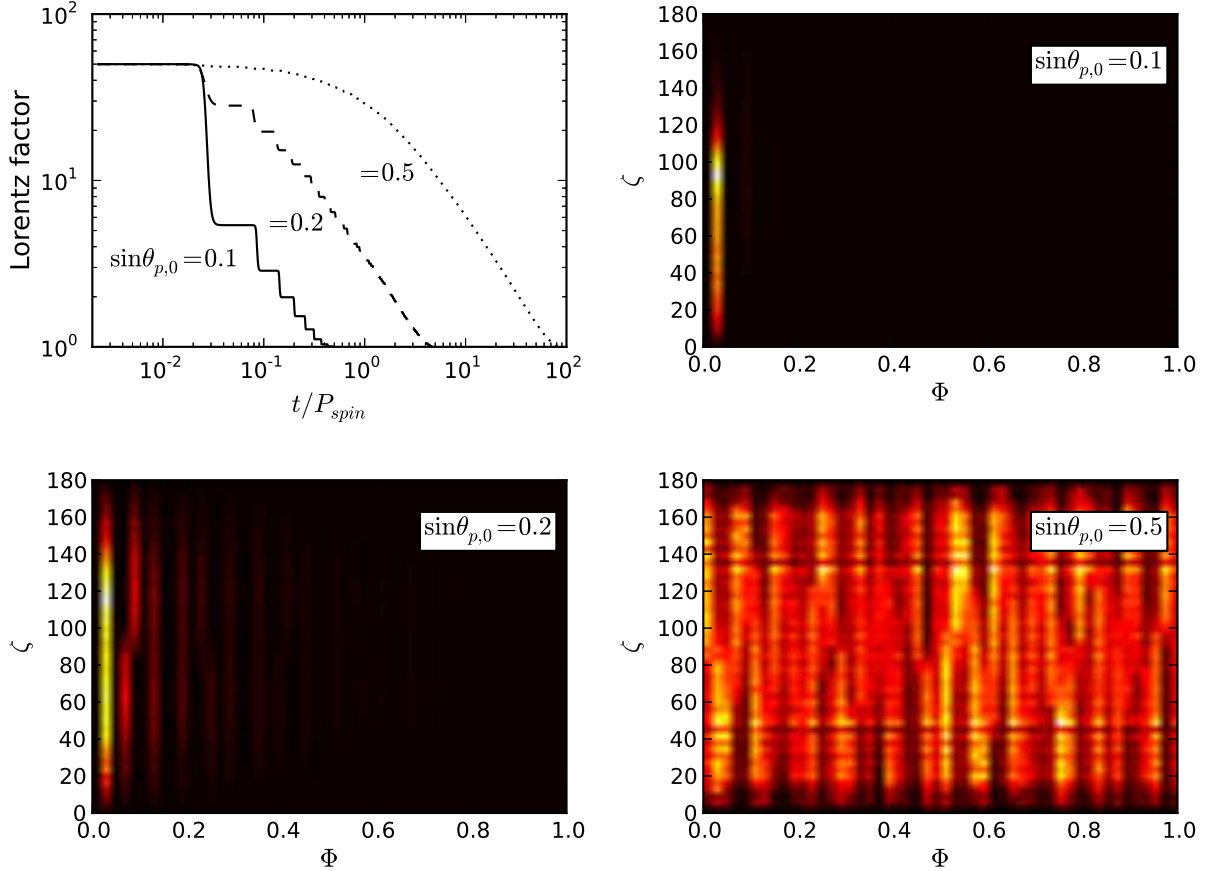


Fig. 4.— Sky map of observing angle (ζ) and spin phase (Φ) for the electron injected with the Lorentz factor $\gamma_0 = 50$ and the pitch angle $\sin\theta_{p,0} = 0.1$ for the top right panel, 0.2 for the bottom left panel, and 0.5 for the bottom right panel. The brightness of the color represents the intensity of the observed emission. The electrons are injected from $r = a$ and the equator at $\Phi_0 = 0$. The top left panel shows the evolution of the Lorentz factor as a function of time. The dipole magnetic field with $\alpha = 0^\circ$ is used for the calculation. The effect of the gyration motion is taken into account in the calculation.

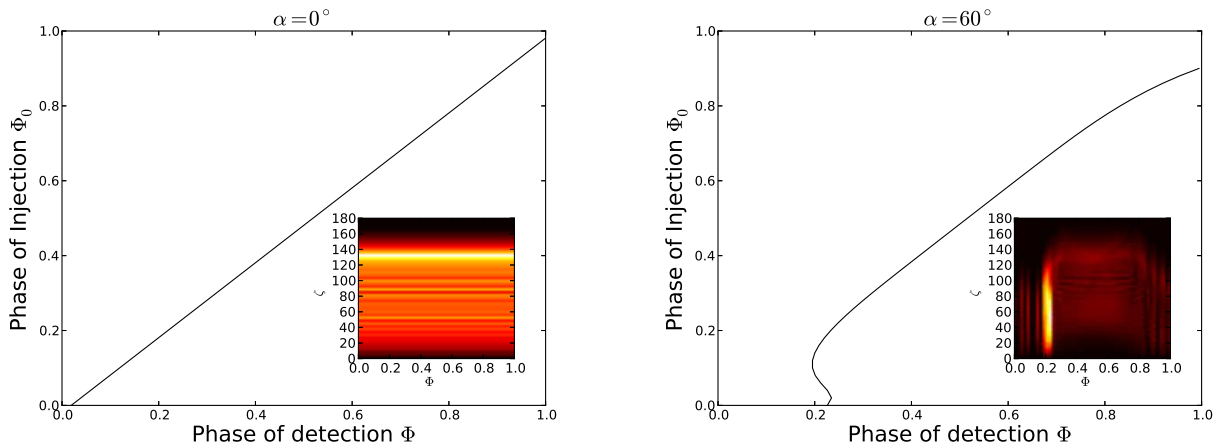


Fig. 5.— Main panel: The relation between the phase of the injection of the electron (Φ_0) and the spin phase of the observed emission from the first mirror point. The initial Lorentz factor and the pitch angle are given by $\gamma_0 = 50$ and $\sin \theta_{p,0} = 0.1$, respectively. In addition, emission from a specific gyration phase is calculated. Inset: sky map of (ζ, Φ) . Emission from all gyration phases is included.

panel), since the most of the electron’s energy is radiated away at the first magnetic mirror point, and the synchrotron emission at subsequent magnetic mirror points is negligible. As a result, the emission from this electron can be mainly observed at narrow spin phase width. For $\sin \theta_{p,0} = 0.2$ (bottom left panel), the magnetic mirror point is located outside of that for $\sin \theta_{p,0} = 0.1$, and hence the synchrotron energy-loss at the first magnetic mirror is less than that for $\sin \theta_{p,0} = 0.1$. As we can see, however, the emissivity at the first magnetic mirror point is still much higher than the emissivity at subsequent mirror points. In our model, therefore, the emission at the first mirror point provides the most contribution on the observed emission from the AR Sco.

For the larger pitch angle with $\sin \theta_{p,0} = 0.5$ (bottom right panel), the electron is trapped at $r \sim a$ and the time scale of synchrotron energy-loss is much longer than the spin period, as the dotted line in the top left panel shows. The emission from this electron covers almost the whole sky, and it may be observed as a nonpulsed emission. Moreover, such an electron whose cooling time scale is longer than the spin period will be absorbed by the companion star after one rotation of the WD and will not contribute much to the observed emission.

Since the WD is spinning, the electrons will be injected on the different magnetic field lines at the different spin phases, that is, Φ_0 in equation (18). We integrate the emission from all magnetic field lines to compare with the observations. As we discussed above, the emission from the first magnetic mirror point of the injected electron mainly contributes to

the observation. In such a situation, we find that the structure of the pulse profile mainly depends on how the spin phase of the detected photon (Φ in equation (18)) is related to the injected phase Φ_0 . If the phase of the detection Φ monotonically shifts with the phase of injection Φ_0 , the predicted pulse profile does not significantly modulate with the spin period. For example, the left panel in Figure 5 shows such a relation calculated with the magnetic inclination $\alpha = 0^\circ$ and the magnetic gyration phase $\delta\phi_g$ in equation (17); the small window in the figure shows the sky map of Φ and ζ with the contribution from the whole gyration phase. Because of the rotation axisymmetric geometry of the magnetic field lines for $\alpha = 0^\circ$, the observed phase Φ monotonically shifts with the injected phase Φ_0 , as the figure shows. As a result, the observed intensity for $\alpha = 0^\circ$ is the constant with the time for any viewing angle ζ .

For a large inclined rotator ($\alpha = 60^\circ$), the phase Φ of the detected photon from the first mirror point does not monotonically shift with the phase of the injection Φ_0 , as the line in the right panel of Figure 5 indicates. We can see in the figure that the photons emitted at the first mirror point by the electrons injected at $0 < \Phi_0 < 0.2$ are observed at a narrower width in the spin phase around $\Phi \sim 0.2$. In the sky map of $\Phi - \zeta$, therefore, the intensity at $\Phi \sim 0.2$ is higher than the intensity at other phases, as the inset in Figure 5 shows. As a result, the observer with an appropriate viewing angle ζ will measure a significant modulation of the emission with the spin period of the WD.

The concentration of the detected photons at the narrower spin phase for the larger inclination angle can be understood as follows. In the present calculation for Figure 5, we inject the electron into the southern hemisphere of the WD’s magnetosphere (Figure 1). At the companion star, the radial direction of the magnetic field of the WD depends on the spin phase. For example, the radial direction at $\Phi_0 = 0$ (the magnetic axis points toward the companion) points to the outer magnetosphere, while at $\Phi_0 = 0.5$ it is directed toward the inner magnetosphere (Figure 1). For the electron injected at $\Phi_0 \sim 0$, it initially moves toward the light cylinder and returns to the inner magnetosphere along the closed magnetic field line, and therefore it takes a longer time, after the injection, to reach the first magnetic mirror point than the electron that is injected at a later time ($\Phi_0 > 0$). This difference in the travel time to the first magnetic mirror point causes an enhancement of the observed emission at the specific spin phase. As we can see in the Figure 5, the emission from the half-hemisphere makes one high-intensity region in the sky map. As we expect, therefore, the contribution from the opposite hemisphere creates another high-intensity region, which separates ~ 0.5 spin phase. The observer whose line of sight cuts through two bright regions in the sky map will measure the double-peak structure in the light curve.

3.3. Application to AR Scorpii

3.3.1. Parameters and assumptions

To apply the model to AR Sco, we assume that the magnetic interaction at the companion star injects the same number of the electrons at the northern and southern hemispheres from the equator of the WD. We represent the results with $\mu_{WD} = 6.5 \times 10^{34} \text{G cm}^3$, $\eta = 1$, and $\delta = 0.01$ in equation (4) and the efficiency $\chi = 10^{-5}$ defined in equation (5). We fit the SED of the AR Sco with $p = 2.5$. With these parameters, the minimum and maximum Lorentz factors are estimated as $\gamma_{min} \sim 50$ and $\gamma_{max} \sim 5 \times 10^6$, respectively. Other important parameters are the inclination angle α and the viewing angle ζ that affect the predicted pulse profile. As we have assumed, the spin axis of the WD is perpendicular to the orbital plane, and the WD is rotating in the same sense as the binary orbit of the companion.

As we discussed in section 3.1, the evolution of the Lorentz factor and the perpendicular momentum of the injected electrons depend on the initial pitch angle. The distribution of the pitch angle of the particles for different acceleration processes has been investigated by the previous authors (Achterberg et al. 2001; Kartavykh et al. 2016), but it is still under investigation with a more realistic situation. In this study, therefore, we assume an isotropic distribution in the initial pitch angle $\theta_{p,0}$, that is,

$$\frac{d\dot{N}_e}{d\theta_{p,0}} = \text{constant}.$$

We note that, in our model, the electrons that are trapped at the close magnetic field line by the magnetic mirror are eventually absorbed by the companion stellar surface after one rotation of the WD. In the calculation, we do not take into account the synchrotron self-absorption, which may be important for the radio band (Geng et al. 2016).

3.3.2. Pulse profile

Figures 6 and 7 summarize the predicted pulse profiles in optical (0.3-1eV) and X-ray (1keV-10keV) energy bands, respectively, at the inferior conjunction of the companion orbit, where the companion star is between the WD and the observer; each panel shows the pulse profile as a function of the magnetic inclination α and the Earth viewing angle ζ . In addition, the each panel shows the pulse profile in the two spin phases of the WD with normalized intensity, and the phase zero (and unity) corresponds to the time when the magnetic axis points toward the observer (Figure 1).

We find that the model with a smaller viewing angle predicts a single pulse profile in the

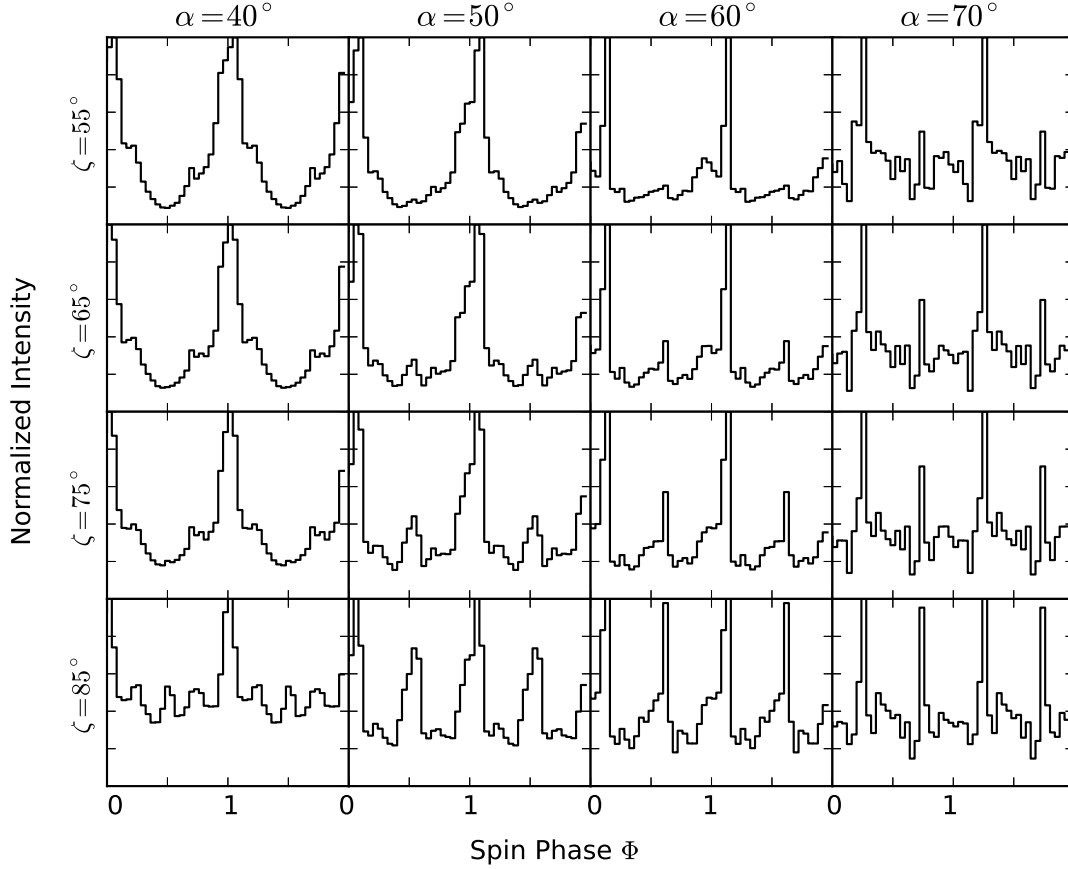


Fig. 6.— Light curve in 0.1-1eV energy bands as a function of the inclination angle (α) and the viewing angle (ζ). The companion star is located between the WD and the observer (inferior conjunction), and the phase zero in each panel corresponds to the time when the magnetic axis points toward the observer. The light curve of two rotations of the WD is represented in each panel.

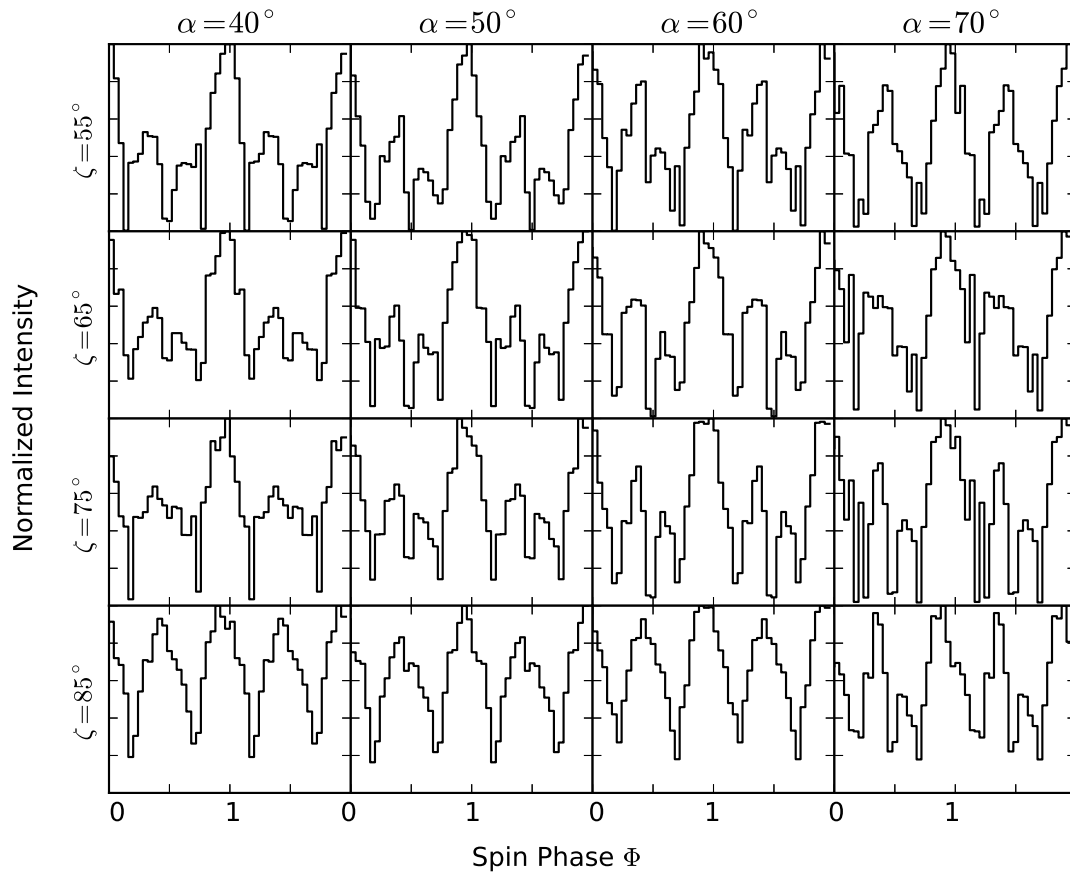


Fig. 7.— Same as Figure 6, but with 1-10keV energy bands.

optical emission, as Figure 6 indicates. For the smaller inclination angle, the observer misses the emission from the half-hemisphere. The optical/UV emission from AR Sco has been observed as the pulsed emission with the sharp double-peak structure in the light curve. In the current model, the double-peak structure can be produced for a larger magnetic inclination and a larger Earth viewing angle. We note that a larger viewing angle of the AR Sco is expected by the observed orbital modulation of the optical emission from the companion star and by a large amplitude of the modulation.

By comparing between Figures 6 and 7, we find that the predicted X-ray pulse is broader and the light-curve structure is more complicate in comparison with the optical light curve. In the current model, the X-rays are produced by the Lorentz factor of $\gamma > 10^4$, for which the synchrotron cooling time scale is comparable to or shorter than the crossing time scale. Unlike the optical emission, therefore, the emission region is not restricted at the first magnetic mirror, but it spreads to a wide space in the WD’s magnetosphere.

3.3.3. *Orbital evolution of the pulse profile*

As we discussed in section 3.2, the pulse peaks are mainly made by the emission of the electrons injected when the magnetic axis of the WD is laid within the plane made by the WD’s spin axis and the companion star. Because of the orbital motion of the companion, therefore, the spin phase of the pulse shifts with the orbital phase. The pulse profile presented in Figures 6 and 7 assumes the geometry in which the companion star is located at the inferior conjunction of the companion orbit, where the companion is between the WD and the observer. Figure 8 compares the pulse profiles of the optical emission at the inferior conjunction, descending node, superior conjunction, and ascending node, respectively, of the companion orbit. The phase zero in all panels corresponds to the time when the magnetic axis points toward the observer. We can see the shift of the pulse peaks and the evolution of the peak intensity with the orbital motion of the companion. We can also see the evolution of the pulse profile along the orbit.

By assuming that the WD is rotating in the same sense as the binary orbit of the companion, we make the time sequence of the calculated intensity for about one orbit and perform the Fourier analysis of it. Figure 9 shows the power spectrum for the global frequency (top left), around the fundamental frequency (top right), around the second harmonic frequency (bottom left), and around the third harmonic frequency (bottom right). In the figure, we can see the peak of the power spectrum around the beat frequency $\nu_B = (1/117\text{s} - 1/3.56\text{hours}) \sim 0.0085\text{Hz}$ and its harmonics, reflecting that the pulse peak monotonically shifts along the orbit. In the figure, we also see that the first harmonic frequency has a stronger power, since

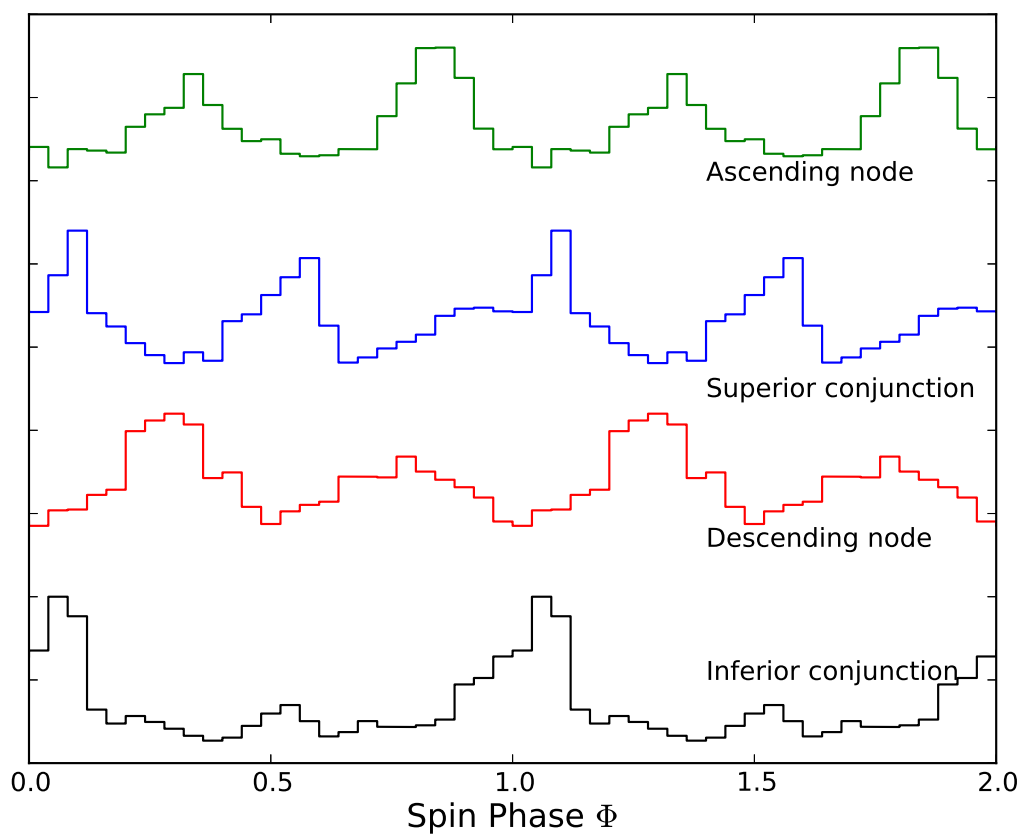


Fig. 8.— Orbital evolution of the pulse profile in the optical bands. The black, blue, red, and green histograms show the pulse profiles at the inferior conjunction, descending node, superior conjunction and ascending node, respectively, of the companion orbit. The phase zero corresponds to the time when the magnetic axis points toward the Earth. The inclination angle and the viewing angle are $\alpha = 50^\circ$ and $\zeta = 65^\circ$, respectively.

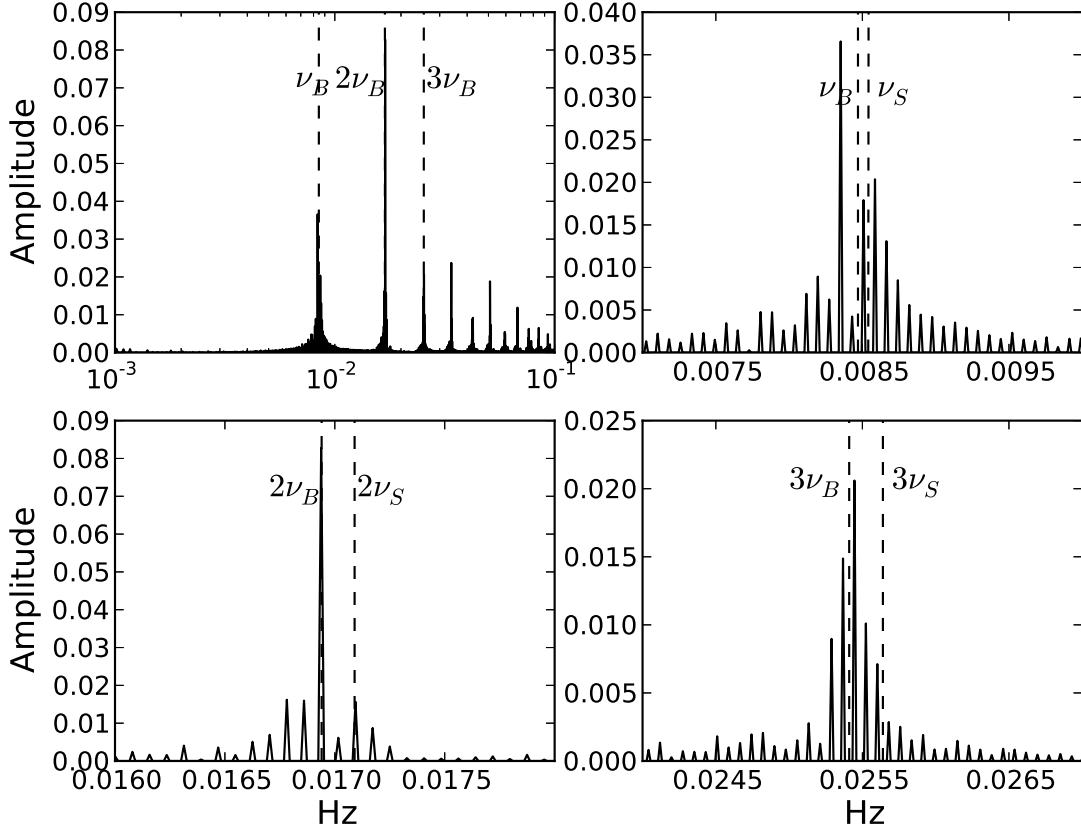


Fig. 9.— Power spectrum of the Fourier analysis for the model light curve calculated with the time of the three orbits. Tot left: global power spectrum. Top right: local power spectrum at the fundamental frequency. Bottom left: local spectrum at around the first harmonic frequency. Bottom right: local spectrum at around the second harmonic frequency. The locations for the fundamental, first harmonic, and second harmonic for the spin and beat frequencies are indicated with the dashed lines in the panels.

the pulse profile has a double-peak structure. These results are consistent with the power spectrum of the optical observations (Marsh et al.2016).

Marsh et al. (2016) reported no significant detection of the pulsed emission in the X-ray bands. It could be due to the shift of the pulse peak with the orbital phase, since the current X-ray instruments cannot resolve the individual pulses of the AR Sco. The time-averaged light curve will be no pulsation or a modulation with a small pulse fraction. We may need a detailed analysis for the timing of arrival of each X-ray photon to detect the pulsation.

3.3.4. Spectrum

Finally, Figure 10 compares the observed SED (Marsh et al. 2016) and model calculations for the different inclination angles: $\alpha = 20^\circ$ (solid), 40° (dashed), 60° (dot-dashed) and 80° (dotted), respectively. In addition, we assume a power-law index of $p = 2.5$ of the injected electrons to explain the broadband spectrum. We take into account the emission of each injected electron up to $t = P$ (one rotation), since the injected electron may be absorbed by the companion star after one rotation of the WD. We can see that the model interprets the global features of the observed SED with the spectral peak at $\sim 0.01\text{eV}$. For $0.1 - 1\text{eV}$, the model flux is smaller than the observed flux. This is because the emission from the companion star contributes to the observed flux in this energy band. In the figure, we can see that the different inclination angle predicts a slightly different model spectrum; the SED of the larger inclination angle has a spectral peak at higher energy. This is because the magnitude of the magnetic field at the first magnetic mirror point tends to be higher for larger inclination angle. We note that the model SED is insensitive to the viewing angle ζ , because the radiation beam from each electron at the mirror point covers a large region in the angle ζ , as Figure 4 shows.

4. Discussion

No concrete evidence of the accretion onto the WD in AR Sco has been found, and it is considered that the system is now in the propeller phase (Beskrovnaya & Ikhsanov 2017). Hence, if there is no flow of accretion matter from the companion star on the open magnetic field line region, the WD could operate the mechanisms of the neutron star (NS) pulsar-like particle acceleration and the nonthermal radiation process in the magnetosphere. In this section, we estimate the flux and typical photon energy of the emission with a simple outer gap model. The outer gap accelerator assumes the particle acceleration around the light

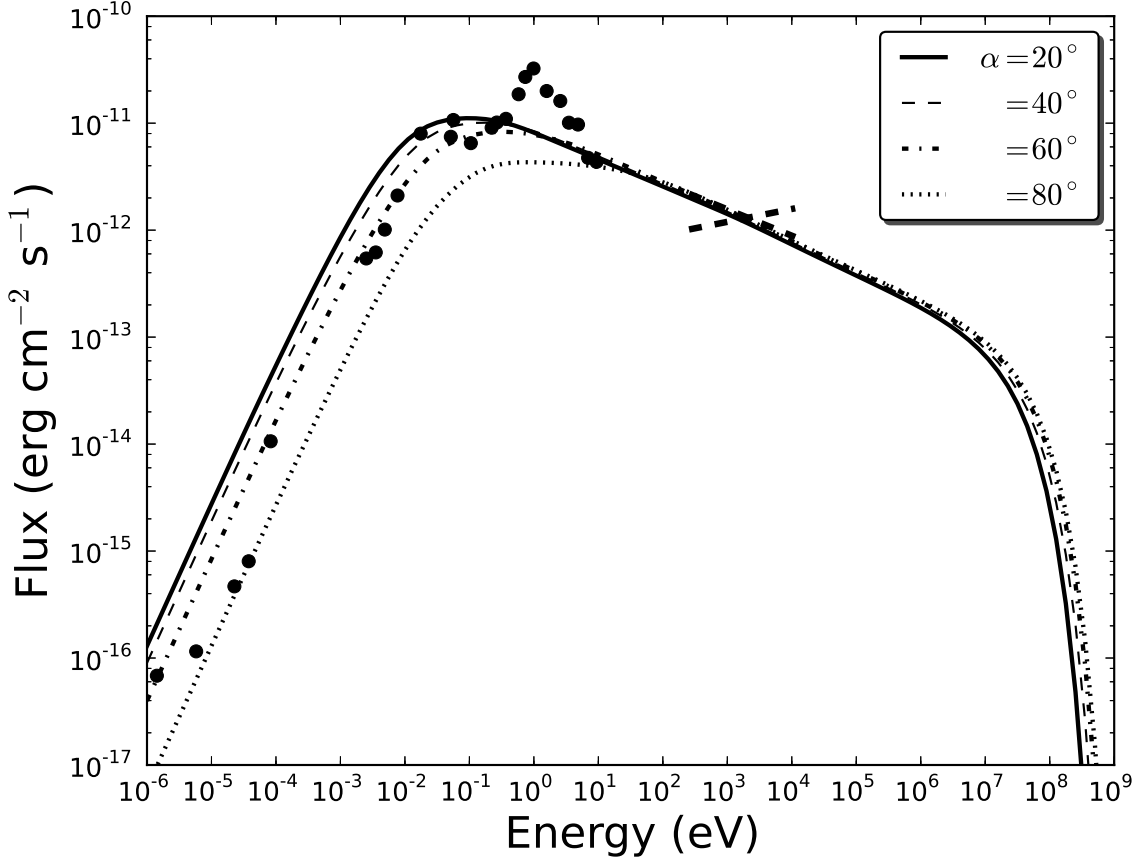


Fig. 10.— Spectrum of ARScorpii. The observational data (filled circles and thick dashed lines) without error bars are taken from Marsh et al. (2016). The different lines show the model calculations for the different inclination angles; $\alpha = 20^\circ$ (solid), 40° (thin-dashed), 60° (dashed-dotted) and 80° (dotted), respectively. In each model calculation, the emission from each electron is taken into account up to the time $t = P$ after the injection. The results are for $\mu_{WD} = 6.5 \times 10^{34} \text{G cm}^3$, $\chi = 10^{-5}$, $\gamma_{max} = 5 \times 10^6$ and $p = 2.5$.

cylinder (Cheng et al. 1986), and it has been considered as the origin of the observed GeV gamma-ray emission from the NS pulsars (Abdo et al. 2013).

With the dipole magnetic field, the polar cap radius of the WD in AR Sco is of the order of

$$R_p = R_{WD} \sqrt{\frac{R_{WD}}{\varpi_{lc}}} \sim 2.5 \times 10^7 \left(\frac{R_{WD}}{7 \cdot 10^8 \text{cm}} \right)^{3/2} \text{ cm}.$$

For the pulsar electrodynamics, the electric current emerges from the polar cap and is circulating in the open field region. The magnitude of the total electric current will be given by the Goldreich-Julian value, $I_{GJ} \sim \Omega_{WD} \mu_{WD} / 2\varpi_{lc}$, (Goldreich & Julian 1969). The electric current running through the outer gap is of the order of

$$I_{gap} \sim f_{gap} I_{GJ},$$

where $f_{gap} (< 1)$ is the fractional gap thickness, which is defined by the ratio of the angular size of the gap thickness measured on the stellar surface to the angular size of the polar cap $\theta_p = \sqrt{R_{WD}/\varpi_{lc}}$.

Using the fractional gap width f_{gap} , the available electric potential drop in the outer gap is of the order of

$$V_{gap} = f_{gap}^2 V_a$$

where $V_a = \mu_{WD} / (2\varpi_{lc}^2)$ is the electric potential difference between the magnetic axis and the rim of the polar cap. The current carrier is accelerated in the outer gap by the electric field parallel to the magnetic field line. For the outer gap region, the typical magnitude of the electric field can be estimated as

$$E_{||} \sim \frac{V_{gap}}{\varpi_{lc}/2} \sim f_{gap}^2 \frac{\mu_{WD}}{\varpi_{lc}^3}. \quad (19)$$

For the outer gap accelerator, the accelerated particles lose their energy via the curvature radiation process and the IC process. The evolution of the Lorentz factor (Γ) of an electron along the magnetic field line may be written as

$$m_e c^2 \frac{d\Gamma}{dt} = eE_{||}c - P_{curv} - P_{IC}, \quad (20)$$

where P_{curv} and P_{IC} are the energy-loss rate of the curvature radiation and the IC process, respectively. The loss rate of the curvature radiation is given by $P_{curv} = 2e^2 c \Gamma^4 / (3R_c^2)$ with R_c being the curvature radius of the magnetic field line. For an isotropic soft-photon field, the energy-loss rate of the IC process is calculated from

$$P_{IC} = \int \int (E_\gamma - E_s) \frac{\sigma_{IC} c}{E_s} \frac{dN_s}{dE_s} dE_s dE_\gamma,$$

where E_γ and E_s are the energies of the scattered and seed photons, respectively, and dN_s/dE_s is the soft-photon field distribution. The cross section is described by

$$\sigma_{IC} = \frac{3\sigma_T}{4\Gamma^2} \left[2q \ln q + (1+2q)(1-q) + \frac{(\Gamma_q q)^2(1-q)}{2(1+\Gamma_q q)} \right],$$

where $\Gamma_q = 4\Gamma E_s/m_e c^2$, $q = E_0/[\Gamma_q(1-E_0)]$ with $E_0 = E_\gamma/\Gamma m_e c^2$ and $1/(4\Gamma^2) < q < 1$ (Blumenthal & Gould 1970).

For the NS pulsar, the IC loss in the outer gap is negligible, and the electric force is immediately balanced with the radiation drag force of the curvature radiation. The saturated Lorentz factor is defined by equating between the acceleration term and the decelerating term on the right-hand side of equation (20),

$$\Gamma_{sat} = \left(\frac{3R_c^2 E_{||}}{2e} \right)^{1/4} \sim 5 \times 10^7 f^{1/2} \left(\frac{\varpi_{lc}}{3 \cdot 10^8 \text{cm}} \right)^{-1/4} \left(\frac{\mu_{NS}}{10^{30} \text{G} \cdot \text{cm}^3} \right)^{1/4}, \quad (21)$$

where μ_{NS} is the magnetic moment of the NS and we assume $R_c \sim \varpi_{lc} \sim 3 \times 10^8 \text{cm}$. In the case of the saturated motion, the luminosity of the emission from the outer gap is of the order of

$$L_\gamma \sim I_{gap} \times \delta\Phi_{gap} \sim f^3 L_{sd},$$

where L_{sd} is the spin-down power of the NS.

For AR Sco, we can see that the IC energy-loss can be comparable to or stronger than the curvature radiation energy-loss. In the Thomson limit of the IC process, the energy-loss ratio of the two radiation processes of AR Sco becomes

$$\frac{P_{IC}}{P_{curv}} = \frac{4\sigma_T c \Gamma^2 U_{ph}/3}{2e^2 c \Gamma^4 / (3R_c^2)} \sim 1 \left(\frac{R_c}{\varpi_{lc}} \right)^2 \left(\frac{U_{ph}}{5 \cdot 10^{-4} \text{erg cm}^{-3}} \right) \left(\frac{\Gamma}{3 \cdot 10^7} \right)^{-2}, \quad (22)$$

where U_{ph} is the energy density of 0.01-1eV photons around the light cylinder of the WD.

The saturated motion of the Lorentz factor is achieved when the maximum Lorentz factor accelerated by the electric potential drop V_{gap} is larger than the saturated Lorentz factor, that is, $eV_{gap}/m_e c^2 > \Gamma_{sat}$. For the AR Sco, the saturation of the Lorentz factor will be achieved when the fractional gap thickness satisfies the condition that

$$f_{gap} > 1.4 \left(\frac{\mu_{WD}}{10^{35} \text{G cm}^3} \right)^{-1/2} \left(\frac{\varpi_{lc}}{5.6 \cdot 10^{11} \text{cm}} \right)^{5/6}, \quad (23)$$

when the curvature radiation is the main energy-loss and

$$f_{gap} > 12 \left(\frac{\mu_{WD}}{10^{35} \text{G cm}^3} \right)^{-1/2} \left(\frac{\varpi_{lc}}{5.6 \cdot 10^{11} \text{cm}} \right)^{1/2} \left(\frac{U_{ph}}{5 \cdot 10^{-4} \text{erg cm}^{-3}} \right)^{1/2}, \quad (24)$$

when the IC process is the main energy-loss. Since f_{gap} should be less than unity, no saturation motion in the our gap accelerator will be realized for the WD in the AR Sco.

For the NS pulsar, the fractional gap thickness will be determined by the pair-creation process between the gamma rays from the curvature radiation process and the background X-ray from the stellar surface (Takata et al. 2012). For the WD pulsar, on other hand, the fractional gap thickness could be determined by the photon-photon pair creation process of the TeV photon from the IC process. The optical depth of the TeV photon is estimated as $\tau_p \sim \sigma_{\gamma\gamma} n_{opt} \varpi_{lc} \sim 10^{-3} (n_{opt}/10^{10} \text{cm}^{-3})$, where $\sigma_{\gamma\gamma} \sim \sigma_T/3$ is the cross section of the pair-creation and n_{opt} is the number density of the $\sim 1\text{eV}$ photon around the light cylinder. For the WD in AR Sco, the fractional gap thickness $f_{gap} \sim 1$ is required to produce TeV photons in the outer gap (Figure 12). If a part of the open field line region is occupied by the matter from the companion star, the possible fractional gap thickness is less than unity. Because of the theoretical uncertainties, we parameterize the fractional gap thickness in this section.

Figure 11 summarizes the integrated flux (left panel) measured on the Earth and the peak photon energy (right panel) of the curvature radiation process in the outer gap of AR Sco as a function of the gap fraction f_{gap} ; in the figure, the solid and dashed lines show the results for the magnetic moment of $\mu_{WD} = 3 \times 10^{34} \text{G cm}^3$ and 10^{35}G cm^3 , respectively, and the solid angle of 4π rad is assumed. The figure indicates that if the gap fraction is larger than $f_{gap} \sim 0.7$, the future hard X-ray/soft gamma-ray missions would measure the curvature radiation from the AR Sco. With a magnetic moment $\mu_{WD} \sim 10^{35} \text{G cm}^3$, for example, the flux measured on the Earth will be 10^{-12}erg/cm^2 and the peak photon energy of the spectrum is in $E = 0.1 - 10 \text{MeV}$ for $f_{gap} > 0.7$. This sensitivity could be achieved by the future hard X-ray/soft gamma-ray missions.

The soft X-ray emission from AR Sco is observed with a flux $F \sim 5 \times 10^{-12} \text{erg cm}^{-2} \text{s}^{-1}$ (Marsh et al. 2016), and it will not be the origin of the outer gap. The current model predicts the gap fraction $f_{gap} \sim 0.3$ to produce the soft X-ray with the curvature radiation process. With $f_{gap} \sim 0.3$, however, the predicted flux is much smaller than the observation. If the fractional gap width is $f_{gap} < 0.2$, the peak photon energy of the outer gap emission is located in the optical band. In such a case, however, the outer gap emission is buried under the emission from the trapped electrons/stellar emission discussed in the previous sections.

Figure 12 shows the predicted flux measured on the Earth and the peak photon energy of the IC process of the outer gap. As we can see in Figure 12, the IC process produces $> 0.1 \text{TeV}$ photons if the gap fraction is $f_{gap} > 0.3$. Moreover, for $f_{gap} > 0.5$, the expected flux is $> 10^{-13} \text{erg cm}^{-2} \text{s}^{-1}$, which would be measurable by the future CTA observation.

In summary, we discussed the radio/optical/X-ray emission from AR Sco. In our model, the magnetic dissipation process on the M star surface produces (i) an outflow from the companion star, (ii) heating of the companion star surface, and (iii) acceleration of the electron to relativistic energy. The accelerated electrons, whose typical Lorentz factor is $\gamma_0 \sim 50$, are trapped in the close magnetic field lines. We solved the motion of the trapped electrons along the magnetic field under the effects of the synchrotron loss and the first adiabatic invariance. We found that the electron injected toward the WD's surface with a pitch angle of $\sin \theta_{p,0} \geq 0.05$ is trapped at the closed magnetic field lines by the magnetic mirror effect. For such an electron, most of the initial energy is released at the first mirror point by the synchrotron radiation process. We demonstrated that for the inclined rotator with the dipole magnetic field, the synchrotron emission from the trapped electrons injected at the different spin phase can create the light curve with a double-peak structure, which is consistent with the observations. The model expects that the pulse profile is linearly shifts with the orbital phase, and this shift is observed as the beat frequency in the spectral power of the Fourier analysis. The model interprets the global features of the observed SED in radio to X-ray energy bands. We discussed the curvature radiation and the IC process in the outer gap accelerator of the WD in AR Sco. The curvature radiation from the outer gap could be measured by the future hard X-ray and soft gamma-ray missions, if the gap fraction is $f_{gap} > 0.7$. The TeV emission via the IC process from AR Sco may be also detected by the future CTA project.

We express our appreciation to an anonymous referee for useful comments and suggestions. We thank to Drs. Lin, L.Chen-Che and Hu, Chin-Ping for useful discussion on the timing analysis. J.T. and H.Y. are supported by NSFC grants of Chinese Government under 11573010, U1631103, and 11661161010. K.S.C. is supported by GRF grant under 17302315.

REFERENCES

- Abdo, A. A.; Ajello, M.; Allafort, A.; Baldini, L.; Ballet, J.; Barbiellini, G.; Baring, M. G.; Bastieri, D., 2013, *ApJS*, 208, 17
- Achterberg, Abraham; Gallant, Yves A.; Kirk, John G.; Guthmann, Axel W., 2001, *MNRAS*, 328, 393
- Angel, J. R. P., Liebert, J., Stockman, H. S., 1985, *ApJ*, 292, 260
- Beskrovnaya, N. G.; Ikhsanov, N. R., 2017, Proceedings of a conference held at Special Astrophysical Observatory, Astronomical Society of the Pacific, p.439, arXiv:1612.07831
- Blumenthal, George R.; Gould, Robert J., 1970, *RvMP*, 42, 237

- Buckley, D. A. H.; Meintjes, P. J.; Potter, S. B.; Marsh, T. R.; Gänsicke, B. T., 2017, *NatAs*, 2017, 1, 29
- Cheng, Andrew F., 1989, *ApJ*, 339, 291
- Cheng, K. S.; Ho, C.; Ruderman, M., 1986, *ApJ*, 300, 500
- de Jager, O. C., 1994, *APJS*, 90, 775
- de Jager, O. C.; Meintjes, P. J.; O’Donoghue, D.; Robinson, E. L., 1994, *MNRAS*, 267, 577
- Ferrario, L., de Martino, D., Gänsicke, B. T., 2015, *SSRv*, 191, 111
- Frank, J., King, A., & Raine, D. 2002, *Accretion Power in Astrophysics* (Cambridge: Cambridge Univ. Press)
- Fruchter, A. S.; Gunn, J. E.; Lauer, T. R.; Dressler, A., 1988, *Nature*, 334, 686
- Geng, Jin-Jun; Zhang, Bing; Huang, Yong-Feng, 2016, *ApJL*, 831, 10
- Harding, Alice K.; Usov, Vladimir V.; Muslimov, Alex G., 2005, *ApJ*, 622, 531
- Holberg, J. B., Oswalt, Terry D., Sion, E. M., 2002, *ApJ*, 571, 512
- Ikhsanov, N. R.; Neustroev, V. V.; Beskrovnaya, N. G., 2004, *A&A*, 421, 1131
- Ikhsanov, N. R. 1998, *A&A*, 338, 521
- Kanbach, G.; Słowikowska, A.; Kellner, S.; Steinle, H., 2015, *AIPC*, 801, 306
- Kartavykh, Y. Y.; Dröge, W.; Gedalin, M., 2016, *ApJ*, 820, 24
- Kashiyama, Kazumi; Ioka, Kunihito; Kawanaka, Norita, 2011, *PhRvD*, 83, 3002
- Kemp, J. C., Swedlund, J. B., 1970, *ApJL*, 162, 67
- Kepler, S. O., Pelisoli, I., Koester, D., Ourique, G., Kleinman, S. J., Romero, A. D., Nitta, A., Eisenstein, D. J. et al. 2015, *MNRAS*, 446, 4078
- Kepler, S. O., Pelisoli, I., Jordan, S., Kleinman, S. J., Koester, D., Külebi, B., Peanha, V., Castanheira, B. G. et al. 2013, *MNRAS*, 429, 293
- Kleinman, S. J., Kepler, S. O., Koester, D., Pelisoli, Ingrid, Peçanha, Viviane, Nitta, A., Costa, J. E. S. et al. 2013. *ApJS*, 204, 5

- Kong, A. K. H.; Huang, R. H. H.; Cheng, K. S.; Takata, J.; Yatsu, Y.; Cheung, C. C.; Donato, D.; Lin, L. C. C., et al. 2012 *ApJL*, 747, 3
- Kuiper, L.; Hermsen, W.; Cusumano, G.; Diehl, R.; Schönfelder, V.; Strong, A.; Bennett, K.; McConnell, M. L., 2001, *A&A*, 378, 918
- Lai, Dong, 2012, *ApJL*, 757, 3
- Marsh, T. R.; Gänsicke, B. T.; Hümmerich, S.; Hamsch, F.-J.; Bernhard, K.; Lloyd, C.; Breedt, E.; Stanway, E. R. et al. 2016, *Nature*, 537, 374
- Patterson, Joseph, 1994, *PASP*, 106, 209
- Reiners, A.; Basri, G.; Browning, M., 2009, *ApJ*, 692, 538
- Ritter H., Kolb U., 2010, *VizieR On-line Data Catalog*, 1, 02018
- Roberts, Mallory S. E., 2013, *Proceedings of the International Astronomical Union*, Volume 291, pp. 127-132
- Sion, Edward M., Holberg, J. B., Oswalt, Terry D., McCook, George P., Wasatonic, Richard, Myszkla, Janine, 2014, *AJ*, 147, 129
- Takata, J.; Cheng, K. S.; Taam, Ronald E., 2012, *ApJ*, 745, 100
- Takata, J.; Chang, H.-K.; Cheng, K. S., 2007, *ApJ*, 656, 1044
- Terada, Yukikatsu; Hayashi, Takayuki; Ishida, Manabu; Mukai, Koji; Dotani, Tadayasu; Okada, Shunsaku; Nakamura, Ryoko; Naik, Sachindra, et al., 2008, *PASJ*, 60, 387
- Usov, V.V., 1998, *SvAL*, 14, 258
- van den Heuvel, E. P. J.; van Paradijs, J., 1988, *Nature*, 334, 227
- Wynn, Graham A.; King, Andrew R.; Horne, Keith, 1997, *MNRAS*, 286, 436
- York, Donald G., Adelman, J., Anderson, John E., Jr., Anderson, Scott F., Annis, James, Bahcall, Neta A., Bakken, J. A., et al., 2000, *AJ*, 120, 1579

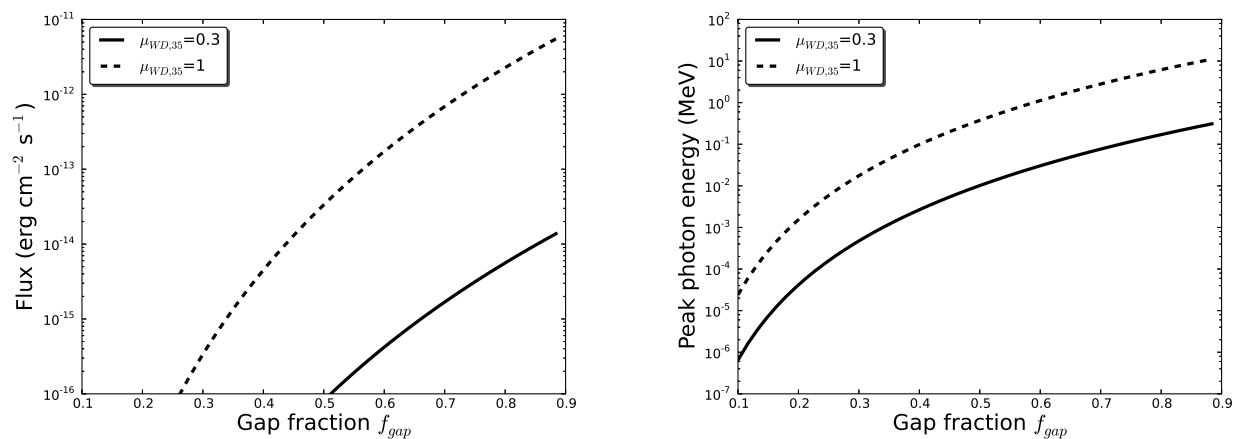


Fig. 11.— Predicted integrated flux (left) and peak photon energy in SED (right) of the curvature radiation process in the outer gap of AR Sco’s WD. The dashed and solid lines are the magnetic moment of $\mu_{WD} = 3 \times 10^{34} \text{G cm}^3$ and 10^{35}G cm^3 , respectively.

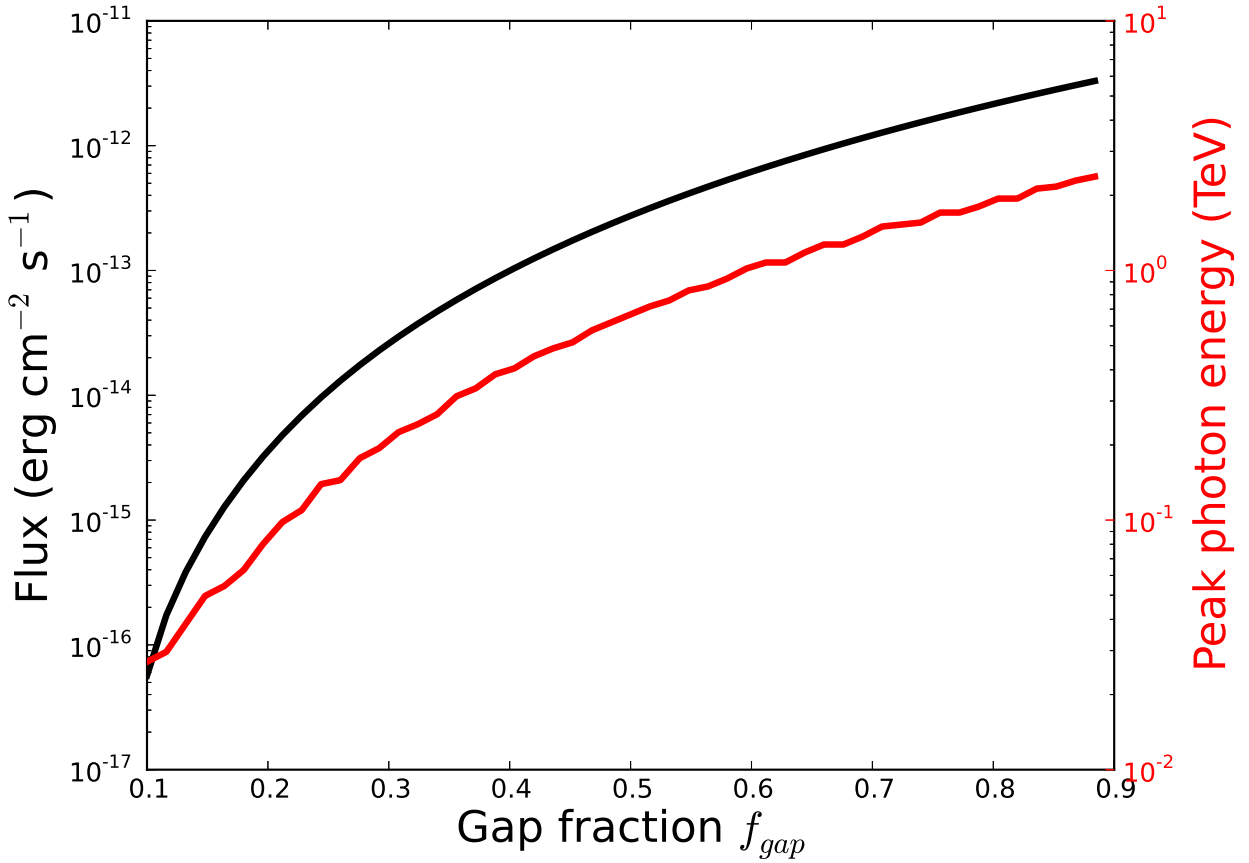


Fig. 12.— Predicted integrated flux (black) and peak photon energy in SED (red) of the IC process in the outer gap of AR Sco’s WD. The magnetic moment is assumed to be $\mu_{WD} = 5 \times 10^{34} \text{G cm}^3$.